HHS Public Access

Author manuscript

Magn Reson Med. Author manuscript; available in PMC 2025 May 19.

Published in final edited form as:

Magn Reson Med. 2024 June ; 91(6): 2431–2442. doi:10.1002/mrm.30029.

Novel pore size-controlled, susceptibility matched, 3D-printed MRI phantoms

Velencia J. Witherspoon[1], **Michal E. Komlosh**[1,2], **Dan Benjamini**[1,3], **Evren Özarslan**[4,5], **Nickolay Lavrik**[6], **Peter J. Basser**[1,2]

[1]Section on Quantitative Imaging and Tissue Sciences, Eunice Kennedy Shriver National Institute of Child Health and Human Development, National Institutes of Health, Bethesda, Maryland, USA

[2]Center for Neuroscience and Regenerative Medicine, Uniformed Services of Health Sciences, Bethesda, Maryland, USA

[3]Multiscale Imaging and Integrative Biophysics Unit, National Institute on Aging, National Institutes of Health, Bethesda, Maryland, USA

[4]Spin Nord AB, Linköping, Sweden

[5]Department of Biomedical Engineering, Linköping University, Linköping, Sweden

[6]Center for Nanophase Materials Sciences, Oak Ridge National Laboratory, Oak Ridge, Tennessee, USA

Abstract

Purpose: We report the design concept and fabrication of MRI phantoms, containing blocks of aligned microcapillaires that can be stacked into larger arrays to construct diameter distribution phantoms or fractured, to create a “powder-averaged” emulsion of randomly oriented blocks for vetting or calibrating advanced MRI methods, that is, diffusion tensor imaging, AxCaliber MRI, MAP-MRI, and multiple pulsed field gradient or double diffusion-encoded microstructure imaging methods. The goal was to create a susceptibility-matched microscopically anisotropic but macroscopically isotropic phantom with a ground truth diameter that could be used to vet advanced diffusion methods for diameter determination in fibrous tissues.

Methods: Two-photon polymerization, a novel three-dimensional printing method is used to fabricate blocks of capillaries. Double diffusion encoding methods were employed and analyzed to estimate the expected MRI diameter.

Correspondence Velencia J. Witherspoon, Section on Quantitative Imaging and Tissue Sciences, Eunice Kennedy Shriver National Institute of Child Health and Human Development, National Institutes of Health, Bethesda, MD, USA. velencia.witherspoon@nih.gov; vwitherspoon@tulane.edu.

CONFLICT OF INTEREST STATEMENT

The authors declare no potential conflict of interest.

SUPPORTING INFORMATION

Additional supporting information may be found in the online version of the article at the publisher’s website.

Results: Susceptibility-matched microcapillary blocks or modules that can be assembled into large-scale MRI phantoms have been fabricated and measured using advanced diffusion methods, resulting in microscopic anisotropy and random orientation.

Conclusion: This phantom can vet and calibrate various advanced MRI methods and multiple pulsed field gradient or diffusion-encoded microstructure imaging methods. We demonstrated that two double diffusion encoding methods underestimated the ground truth diameter.

Keywords

anisotropic phantom; DDE; diameter; DTI; random orientation

1 | INTRODUCTION

Microstructure imaging methods are employed in biological and clinical applications. In the former, these include elucidating features of brain structure and organization, often used to determine anatomical connectivity, for instance, in neuroscience. In the latter case, these include assessing normal and abnormal developmental processes, pathological tissue states, or following features of normal and abnormal aging or detecting trauma, inter alia. These methods seek to use macroscopic scale diffusion-weighted imaging, among others, in conjunction with physical models of the underlying diffusion process at finer length scales, to infer key microstructural features and morphological parameters, often in white matter, such as mean axon diameter (e.g., in CHARMED) or dPFG (double Pulsed Field Gradient) MRI[1,2] or the axon diameter distribution (ADD), for example, in AxCaliber MRI,[3] and potentially restricted domains, in DKI,[4] and MAP-MRI.[5] There is a critical need to design and create MRI phantoms to test and calibrate these and other imaging methods and models and vet their associated data processing and display pipelines. Generally, MR phantoms play a crucial role in vetting data acquisition and analysis pipelines, ensuring that model results conform to experimental data. In clinical and preclinical scanners, MRI phantoms can be used to help ensure quality control, the precision and accuracy of MRI data in single subjects, as well as in longitudinal and in multi-site studies[6] by testing whether they recapitulate the “ground truth” when methods are subjected to data obtained from structures with well defined morphological features, that is, pore size and shape, connectivity, etc. As diffusion-related parameters are increasingly applied to assess more complex morphologies, it is vital to evaluate the performance of these methods on model phantom/material systems that mimic these features, but are simple enough that analytical or approximate solutions can be found to describe the signal attenuation profiles measured.

In attempting to infer features of gray matter, in which there are many crossing processes and myelinated and unmyelinated axons oriented somewhat randomly, there is a need to develop MR techniques that can interrogate these powder-averaged microscopically anisotropic structures. Models and experimental pipelines used to estimate pore size distributions in such complex media require the development of phantoms.[7] Since Cheng and Cory[8] first described and measured microscopic anisotropy within an emulsion of randomly oriented ellipsoidal yeast cells, numerous studies have investigated the relationship between the mPFG diffusion signal attenuation profile on pulse sequence parameters and microstructural features, such as distributions of compartment shape,

size, and orientation.[9] Grebenkov's development of the multiple correlation function framework[9,10] has led to the study of simple pore geometries and arbitrary orientations from diffusion signals, teasing out features of microscopic anisotropy in powder-averaged structures. In attempting to carry-over these methods to microstructure MRI in tissue, particularly in vivo, we must be able to calibrate MRI scanners and standardize instrument performance.

The use of designer phantoms greatly aids in this process. Several MRI phantoms, Table S1, have been designed and fabricated[11-18] to represent microscopically anisotropic powder averaged structures. Although functional, they often suffer from susceptibility artifacts, safety concerns, like spillage of organic solvents, or fragility, limiting phantom transportability and robustness. If there are large susceptibility differences between the phantom materials and the imbibing liquid, the estimates of the ground truth diameter can be compromised.[19,20] Therefore an ideal restriction-based diffusion phantom mimics the geometrical feature of the tissue morphology of interest and is comprised of a material that is well-matched to its imbibing liquid. If the imbibing liquid should also be nonvolatile, FDA-approved, and safe for technicians to handle in the case of spillage, water is ideal for such a phantom design. We aim to simultaneously address the issues of susceptibility, fragility, and robustness by employing advanced three-dimensional (3D) printing technology. We hypothesize that this method comprising high-accuracy and precision fabrication techniques can be utilized to produce MRI phantoms that are microscopically anisotropic, can be randomly oriented to exhibit powder averaging, and are comprised of a material with magnetic susceptibility values very close to water's, thus, providing model systems mimicking important aspects of the anisotropic microcapillary-like structures (10 μm) found in gray and white matter in the central nervous system (CNS) and peripheral nervous system (PNS), as well as skeletal muscle. Additionally, we provided examples of its usefulness by employing double diffusion acquisition methods that were specifically developed to detect microscopic anisotropy and showing that there is room for improvement of both the phantom and models by incorporating the effects of surface relaxivity.

2 | METHODS

2.1 | 3D printed phantom

MRI Phantoms were printed using a Photonic Professional GT stereolithography tool based on 2-photon polymerization (Nanoscribe, GmbH) at the Center for Nanophase Materials Sciences (CNMS) at Oak Ridge National Laboratory (ORNL). The 3D computer-assisted designs of microcapillary arrays arranged with hexagonal packing within 300 μm × 300 μm × 300 μm cube/blocks were compiled using the 3D graphic editor built into COMSOL Multiphysics software (Figure S1). Hexagonal packing and the smallest feasible inter-capillary distances were used to maximize the total pore volume and thus the signal-to-noise ratio (SNR) in MRI. Four small parallelopipeds were added to the bottom side of each block to elevate capillary arrays and facilitate the removal of un-crosslinked photo-resin from the high-aspect-ratio capillaries during the development step. The compiled 3D computer-assisted designs file of capillary arrays was saved in the STL format and subsequently

imported into DeScribe software (Nanoscribe GmbH) to compile job files with various printing parameters tabulated in Table 1.

Power, slicing, hatching, and 3D printing process parameters were varied and optimized in order to produce blocks with solid and smooth walls between adjacent capillaries. To meet the requirement of the targeted 10 μm inner diameter (ID), diameters of capillaries in the final computer-assisted designs were adjusted after several iterative printing tests. IP-S photo-resin, a poly (methyl methacrylate) based formula, (Nanoscribe, GmbH) was used for all printing tasks.

This specific combination of resin and printer was chosen because it could yield high-resolution prints and small tolerances (±100nm). The final design was intended to meet the above criteria for capillary arrays of 10 μm ID, contained within cube/blocks of 300 μm × 300 μm × 300 μm as shown in Figure S1. To produce total capillary volumes sufficient for MRI characterization, job files contained step-and-repeat loops compiled in such a way that each sample contained 7×7 to 15×15 2D arrays of individual blocks shown in Figure S1 in the Supplementary Material. 150 μm thick circular coverslips or 500 μm thick silicon chips were used as substrates for printing. Development of the printed structures was carried out in 1-methoxy-2-propyl acetate for at least 24 h with subsequent rinsing in isopropanol and drying in a gentle stream of filtered dry nitrogen. A 24- to 48-h development time was found to be necessary to ensure complete removal of the uncrosslinked IP-S photoresin from the high-aspect-ratio capillaries.

2.2 | Microscopy characterization and sample preparation

Scanning electron microscopy (SEM) images were taken before and after the MRI experiments on a Hitachi instrument. The blocks were coated with a 5- to 10-nm layer of gold when imaged after the MRI acquisition. Images were then analyzed with ImageJ to determine the microscopic pore size distribution. Blocks were plasma treated to clean the surface of residual organic matter, then loaded with water in an NMR tube. Sonication and vacuum for 5–7 days were performed to de-gas samples and to eliminate artifact-causing air bubbles, and the sample was then sealed for imaging. Susceptibility-matched plugs were placed at the bottom of the glass tube and on top of the sample, preventing movement of the blocks during the experiment while suppressing susceptibility gradients at the top and bottom surfaces of the phantom.

2.3 | MRI measurements and analyses

3D printed capillary blocks were removed from their support, randomly distributed in a glass tube, loaded with H_2O, and remeasured using a diffusion tensor imaging (DTI)[21] protocol with a 3D-EPI (echo-planar imaging) acquisition with the experimental details briefly described here; 21 directions, at b-values of 200, 400, 1200 s/mm^2 with $b = \gamma^2\delta^2G^2\left(\Delta - \frac{\delta}{3}\right)$, where γ is the gyromagnetic ratio, and δ and G denote the duration and amplitude of the gradients, respectively. Eight segments were used with a voxel size of either 50 × 50 × 50 μm^3 , yielding an SNR ≈ 30, or 100 × 100 × 100 μm^3, yielding an SNR of ≈ 70. We used TORTOISE[22,23] to produce Diffusion-Encoded Color (DEC) and Fractional Anisotropy (FA) images from the DTI experiments.

2.3.1 | Double pulsed field gradient MRI: The parameters, TE, δ, and Δ, were kept constant at 35, 3, and 30 ms, respectively. For the aligned phantom, the voxel size was 50 × 50 × 200 μm^3. The angle between the two diffusion blocks was varied from 0 to 360° in intervals of 15° in the plane of restriction of the capillary array, totaling 24 angles,[24] with q values ranging from 0 to 5.73 × $10^4 m^{-1}$. A semianalytical model[9] for gradient waveforms encoding diffusion in multiple directions was employed in the analysis.

To obtain the phantom with randomly oriented cylinders, the blocks were removed from their support and suspended in a 4-mm glass tube. This phantom was scanned using a dPFG MR sequence,[25] acquiring the data on five shells with q-values ranging from 0 to 8.5947 × 10^4 m^{-1}. Data were collected with either t_m=0 or 6 ms with a voxel size of 100 μm^3, yielding a SNR of ≈ 71.5. We employed a two-compartment (free and restricted diffusion) data analysis model. For the signal from water trapped within cylinders, the following expression was obtained by extending the previous works[26-28] to randomly distributed cylinders:

$$\bar{E}(g,\psi) = \sqrt{\pi} e^{-m_a} \sum_{n=0}^{\infty} \binom{2n}{n} \frac{(m_b)^{2n}}{2^{2n+1}} \frac{{}_1F_1\left(2n+1; 2n+\frac{3}{2}; m_c\right)}{\left(2n+\frac{1}{2}\right)!}. \quad (1)$$

Here, $E(g,\psi)$ is the signal attenuation with g being the gradient magnitude and ψ is the angle between the gradients employed in the two encoding blocks. The quantities m_a and m_b depend on the experimental parameters Δ, δ, and ψ as well as the bulk diffusivity and the cylinder radius to be estimated. The details of the above expression and its derivation are described in Appendix S1. We employed a Levenberg–Marquardt nonlinear least-squares fitting algorithm (available at https://github.com/segasai/astrolibpy/blob/master/mpfit/mpfit.py) to estimate the apparent cylinder diameter, the intracylinder signal fraction, and the signal with no diffusion attenuation. Only the intracylinder signal fraction was constrained to the interval [0, 1]. The final estimates did not depend on the initialization of these parameters. For both the free and restricted compartments, the bulk diffusivity of water was set to 1.85 × 10^{-9} m^2 s^{-1} based on the known free diffusivity of water at the sample temperature of 16°C.

2.3.2 | Nondiffusion MRI measurements: Inversion Recovery preparations with EPI acquisition and fast low-angle shot (FLASH3D) experiments were used to produce high-resolution T_1 maps, while multislice multi-echo sequence was utilized to produce T_2 maps, and multigradient echo acquisition was used to produce a T_2^* map. The measured relaxation time constants were used to set and constrain the diffusion time and echo time. Additionally, diffusion-weighted (DW) T_1 maps and DW T_2 maps with b-values of 300 s/mm^2 were measured by combining a pulsed-field gradient spin echo block with either an inversion recovery preparation sequence with an EPI acquisition and/or varying the echo time.[29] The T_1 weighted images were acquired with a 250 ms recovery time. The images were analyzed to generate a T_1 map using a custom MATLAB code. The T_2 weighted image was acquired with an echo time of 83 ms. Diffusion-filtered relaxation experiments were used to understand the relaxation behavior of the diffusing spins. These were acquired to

isolate the relaxation behavior of the proton signals that would contribute to both d-PFG and DTI experiments. Thus, nondiffusing spins do not contribute to the calculated values for these maps. The experimental parameters can be found in Table S2. multislice multi-echo sequence, multigradient echo, and inversion recovery experiments with varied echo and delay times were analyzed to generate T_2 T_2^*, T_1 maps by custom MATLAB code, where the voxelwise relaxometry decays were fitted to a mono-exponential with a constant baseline using a nonlinear least-squares fitting routine to identify the best fit time constants.

The phantom with randomly distributed blocks was scanned using a standard Point RESolved Spectroscopy (PRESS) sequence to assess if the phantom region was subject to orientation-dependent field distortions, where the volumes for individual experiments were registered to different block orientations and regions of interest were identified via DTI. To qualify how the phantom material's susceptibility may affect diffusion imaging, we conducted multiple EPI experiments varying the number of segments and quantitatively compared the images to one another. Summarized experimental data and parameters can be found in Table S2. All MRI measurements were performed on a 7T Bruker MRI scanner with an Avance III spectrometer and a Micro2.5 microimaging probe with a 5-mm ^{1}H RF coil at 16°C.

3 | RESULTS

The tested printing speeds and the resulting wall uniformity are shown in Table 1 and Figure 1C-E. The finalized MRI phantom was printed under the conditions listed in Table 1 for Sample E in Table 1. A series of SEM images for ≈ 36 000 pores were analyzed using ImageJ to calculate the nominal pore size diameter of 10.7 ± 0.3 μm. This print resulted in an array of aligned blocks, see Figure 1, where the gaps between adjacent blocks are approximately 50 μm controlled by thin bridges at the center of each top edge of the block. The combined signal from the 200 μm slice through this array of blocks was fitted to a two-compartment (free and restricted) model to estimate the pore diameter, Figure 2. The resulting voxelwise cylinder diameter estimate is 8.38 with a SD of 1.45 μm for the aligned phantom.

In Figure 3, an axial slice showing high resolution (50×50×50 μm^3) DEC and FA maps calculated from DTI data using the TORTOISE pipeline,[22] are shown. The array of colors in Figure 3A of the (DEC) map[30] shows that the blocks are truly oriented in different orientations yielding a microscopically anisotropic ROI. Panel B in Figure 3 shows blocks (1-11) chosen at random from the center slice where PRESS[31]) was performed to record the chemical shift of the water imbibed in the blocks as a function of orientation. The results for a diffusion-T_1 weighted inversion recovery preparations with EPI acquisition experiment are shown as a T_1 map (A), and T_1-weighted image (B), with non-diffusion weighted inversion recovery preparations with EPI acquisition experiment, showing a T_1-weighted image (C) and T_1 map (D) in Figure 4. The T_1 maps in C and D were plotted with the same magnitude and with calculated T_1 values ranging from 1 to 10^3 ms. DW T_2-weighted image (E) and resulting T_2 map (F) are also shown in Figure 4. The DW block used a spin echo with a b-value of 300 s/mm^2.

The estimates of all quantities are tabulated in Table 2. Figure 5 shows our results from a high-resolution segmented EPI acquisition with varying k-space segments 2, 4, and 8. The 4- and 8-segment images were compared to the 2-segment image using the structural similarity index measure (SSIM) and resulted in high SSIM values of 0.9984 and 0.9661, respectively.

4 | DISCUSSION

At the outset, we sought to incorporate features meeting the basic criteria required for a microscopically anisotropic but macroscopically isotropic phantom. We needed to print a microscopic structure that has high morphological uniformity and exhibits restricted diffusion that would result in high macroscopic diffusion anisotropy (FA > 0.6) and would have a magnetic susceptibility that of water to enable the use of diffusion-weighted 3D EPI and fast acquisition schemes commonly used in clinical settings and at high magnetic field without any imaging or other artifacts. This would ensure that the voxels are easily distinguishable from free water in a basic DTI acquisition. It was desirable for the pore fraction to be as close to its maximum value (72%) as possible and to ensure that the SNR is sufficiently high to enable different models to be robustly fitted to experimental data.

There should be no exchange of water between pores to simplify the model that could be used for validation, although exchange could be included in future phantom embodiments. Such phantoms should also be stable and withstand degradation or change in the MR observables for at least a span of 2 years. Using a simple gradient waveform, we estimate 10 μm to be close to the detection limit for most clinical MRI scanners where the gradient strength is often limited to 100 mT/m and chose this as the initial target ID.[33] The pitch of the capillaries was optimized to ensure structural stability after printing. If the pitch were set close to the value of capillary pore diameter, the blocks would become too frail to handle. The height, width, and depth of the block were determined by the maximum probability that the cubes would have no preferred orientation when dispersed in a liquid.

4.1 | 3D printing design

The main challenge in the 3D printing task was balancing the trade-off between the need for small hatching (raster) and slicing (interlayer) distances in a reasonably short printing time. For instance, the printing time per block was under 10 min for samples C and D in Figure 1. However, these samples had unacceptably rough inner capillary surfaces and noticeably porous inter-capillary walls. Intra-capillary walls were made much smoother and without any noticeable porosity by compiling printing jobs with two added contouring lines (Sample E in Figure 1). Compared to Sample C, this also made printing time two times slower, resulting in 60 h to fabricate a 15 mm × 15 mm array. Because MRI relaxation properties are sensitive to the surface roughness of the samples, we chose a longer printing time to achieve a smoother cylinder wall. As 3D printing technology is rapidly improving with faster methods having high tolerances, it is possible to reduce this printing time in the future using different instrumentation. Additionally, we do not employ surface finishing methods (ball milling, acid wash, vapor polishing, etc.) on the samples. Combining faster printing settings with surface smoothing methods could result in faster manufacturing times. It was previously shown that plasma treating PMMA significantly decreases the observed water

contact angle[34] by removing excess organic matter. This sterilization treatment, combined with sonication, significantly helped overcome the capillary pressures to load the phantom with water (low viscosity, high free diffusivity). However, this increase in hydrophilicity may in principle, lead to the emergence of an immobile population of molecules at the surfaces. However, incorporating an "unattenuated" dPFG signal component to the model employed for randomly oriented cylinders resulted in a very small estimate of the signal fraction for such a population (0.037) without significantly improving the quality of the fits. Thus, the question of whether a population of immobile surface water contributes to the dPFG signal remains unanswered.

There are limits to using two-photon polymerization 3D printing to produce MRI phantoms, such as fabrication time removing sacrificial resin from smaller diameter pores. Both can be overcome with a lower-viscosity resin. There are a number of clear advantages to printing phantoms: reproducibility could encourage MRI sites to have 3D printers on site to print the specific designs for testing; tissue-specific resins could be designed to mimic the relaxation and susceptibility behavior; cross-validation with other noninvasive imaging methods could achieve multimodal phantoms; many of the resins produce highly stable structures that are biologically inert; and the method of 3D printing phantoms can produce modular components that can be adapted to incorporate tissue morphological features.

4.2 | Usefulness for diffusion MRI method validation

These arrays of aligned capillaries conform to analytical models of restricted diffusion in cylindrical pores[2,9,35-37] to which NMR or MRI experiments could be compared where an apparent pore diameter could be estimated using a fitting procedure. If wafers were stacked having a known distribution of pore diameters or IDs, it would be possible to construct a diameter distribution phantom, such as that previously made using glass capillary arrays.[13] In this case, the diameter distribution could be estimated using an empirical distribution, although it would be useful to employ a known parametric model to determine whether experimental and model results are consistent. A limitation to this phantom preparation is that water is present within the capillaries and surrounding the blocks. Previous phantoms like the glass capillary array found in Reference 13 were often loaded with H_2O and dispersed in an H_2O immiscible fluid or vice versa. A desired property to incorporate in the future is to control inter-pore exchange, for example, as a means to calibrate a diffusion exchange spectroscopy NMR or MRI experiments. A clever way to repurpose this phantom for a diffusion exchange spectroscopy experimental calibration is to consider the solvent domain at the ends of the capillaries in which water or another solvent in the tubes is close to the pore opening and thus has time to move into the free water compartment from the pores and *vice versa* during the mixing time of the experiment.[38,39] Mixing time dependence, as well as pore hopping processes, could also be studied. Such experiments can be feasibly done using this phantom.

4.3 | Low magnetic susceptibility difference

It is known that magnetic susceptibility (χ) effects can be significant in porous structures if there is a mismatch between the susceptibilities of the fluid and porous medium. Such is the case in glass capillary arrays.[13] This mismatch exists in our polymeric phantom to

a much lesser extent due to the smaller susceptibility difference between plastic and water. The IP-S photo resin is primarily comprised of PMMA, a material previously shown to have magnetic susceptibility close to water, $\chi_{PMMA} - \chi_{H_2O} = -0.036$ ppm, and was evaluated as a highly compatible MR material.[40] Classical analytical and numerical finite element method models indicate that there would be an induced magnetic field within and around a hollow cylindrical tube which would depend on the orientation of the tube with respect to the main applied magnetic field.[41-43]

With a high aspect ratio, one expects the magnetic field within the tube to be uniform but with dispersion at the ends, causing a spread in the Larmor frequencies proportional to the magnitude of $\Delta\chi$. We consider the $\Delta\chi$ dispersion for the randomly oriented emulsion where an analytical solution for the orientation-dependent effective frequency perturbation, $\frac{\Delta\omega}{\omega_0}$ for a hollow cylinder model is presented in Reference 44 for an infinite cylinder with an inner radius, r_i and an outer radius, r_o, with the azimuthal angle ψ and the polar angle θ is reproduced in Table 3, for a cylinder comprised of a lipid bilayer or a myelin sheath. For our phantom $r_i = 10\,\mu$m and $r_o = 12\,\mu$m. We consider solely the mobile spins, as the immobile ones associated with the solid polymer material have extremely short T_2's and do not contribute to dPFG echo, so we can neglect the contribution of the region $r_i < r < r_o$. The contribution to an orientation-dependent frequency perturbation can only come from spins outside the hollow capillaries, where the wall thickness is $r_o - r_i$ and spin from the adjacent or nearest neighbor capillaries are considered; contributions from spins associated with the extra-block water are orientationally averaged, and therefore negligible. If we estimate the effect of neighboring hollow cylinders considering the spins near the inside wall, $r > r_o \frac{\Delta\omega}{\omega_0} \ll 0.1$ ppm.

This small perturbation is not observed on our current instrument due to the inherent resolution of the RF coil and shimming artifacts. To further investigate this behavior, individually oriented blocks were examined via PRESS voxel-wise spectroscopy, experimentally showing that the susceptibility differences between the H_2O and the phantom material are low as the Larmor frequency does not vary significantly with orientation, std = 50 Hz of the maximum, a typical linewidth for our instrument, although we suspect that at higher fields shimming may become more important, it does not create artifacts during image acquisition at 7T. To further show the lack of susceptibility artifacts influencing image quality, EPI data were acquired with 2,4,8 segments as shown in Figure 5A-C, respectively. When comparing the 6- and 8-segment images to the 2-segment image, they have structural similarity (SSIM) indices[45] of 0.9984 and 0.9661, respectively, demonstrating the absence of susceptibility artifacts.

4.4 | Investigating double pulse field gradient sequences

Our group and others have presented several diffusion MRI methods that take advantage of double diffusion encoding in order to enhance sensitivity to both the size and shape of restriction within the voxel.[46] As a first pass, we chose to apply a double-PFG filter before an EPI acquisition to test the method's ability to characterize the phantom. The results from the aligned phantom are presented in Figure 2, where the first gradient pulse was aligned

with the capillary major axis, and only the azimuth angle between the first and second gradient pulse was varied. All other experimental variables were held constant (see Table S2) with the slice location chosen to exclude the top and bottom edges of the blocks. The short mixing time, $t_m = 0$, data were fitted using the mixed free and restricted diffusion model with the resulting fit shown in Figure 2. The data with widely varied parameters G, ψ, and θ is well-represented by the model, although the estimated diameter, 8.58 μm, is less than the ground truth. In 30 ms, a water molecule travels about 13 μm, which means that a significant portion of the restricted water molecules should have hit a capillary wall at least once. Water outside the cylinders resides in channels that are approximately 50 μm in width. Thus, their motion can be considered free. Our measurements suggest that their contribution to the signal without diffusion attenuation is about 38%. We note that increasing the diffusion time would suppress this signal fraction of the extracapillary water.

For the randomly oriented phantom, we increased the voxel size from 50 μm to 100 μm. As a result, the DTI measurements revealed FA values, which decreased from about 0.8 to about 0.45; see Figure 6A. This reduction is due to the well-known “powder averaging” effect. The resulting estimated diameter map shown in Figure 6C indicates that the mixed model (with one restricted and one free compartment) does not necessarily capture the complexity of the phantom. The model introduced for randomly oriented cylinders also well-represented the signal, though the estimates of the cylinder diameter was once again smaller than its expected value.

There are several factors that could be considered for explaining the discrepancy between the actual diameter of the cylinders as measured from SEM images and that estimated from the fitting of the dPFG models. First, these models assume all cylinders to be the same exact diameter. If there is a distribution of diameters, the larger capillaries have a larger effect on the signal due to their volume. Thus, the apparent pore diameter is expected to be larger than the measured one,[47] which does not offer an explanation for our underestimation. Another potential explanation concerns the bias due to the magnitude signal having a Rician distribution. However, our SNR is relatively high, and the angular profiles, for example, in Figure 7 do not exhibit any Rician noise floor characteristics. Moreover, repeated fitting by excluding the outermost shell(s), which have a lower SNR and would consequently be affected more severely by the Rician bias, resulted in even lower estimates of the ID (7.75 μm if the outermost shell is removed, 7.60 μm if two shells corresponding to the two largest gradient strengths are excluded). Yet another potential explanation is that water could be experiencing surface relaxation effects due to hydrophilic surface interactions that we have not accounted for in our models. Such effects will be investigated in the future.

A significant amount of the signal decay is due to freely diffusing water in our phantoms. For the models explored in this paper, the diameter estimates and the bulk diffusivities are correlated. To weaken this correlation, another liquid having a higher viscosity or an inert small molecule or sol-gelling material could be used in filling the phantom. In the case of diffusion exchange, which is increasingly being understood as a process occurring in gray matter,[48] we plan to use this phantom to vet diffusion exchange spectroscopy[49] methods as in Reference 38.

5 | CONCLUSION

High-resolution 3D printing is creating new opportunities for phantom fabrication including the creation of reproducible, durable, ground-truth structural MRI phantoms that can mimic complex structural features of the tissue. Here, we have shown that phantoms with microscopic pore sizes can be fabricated via 3D printing and filled with water, resulting in a microscopically anisotropic phantom that does not suffer from susceptibility artifacts. Although a single pore size was used here, this method can also produce controlled distributions of pore sizes, varied wall permeabilities, and controlled orientation distributions, which are needed to improve and validate methods that seek to characterize these features in tissues.

Supplementary Material

Refer to Web version on PubMed Central for supplementary material.

ACKNOWLEDGMENTS

A portion of this research was conducted at the Center for Nanophase Materials Sciences, which is a DOE Office of Science User Facility. The authors thank Drs Ye Sun and Christopher Bleck for their electron microscopy technical expertise. SEM imaging was performed on a Hitachi instrument maintained by the NIH, National Heart, Lung, and Blood Institute (NHLBI). VJW and PJB were supported by the Intramural Research Program (IRP) of the *Eunice Kennedy Shriver* National Institute of Child Health and Human Development (NICHD). VJW was also supported by the National Institutes of General Medical Science K99GM140338. MK and DB were supported by the Center for Neuroscience and Regenerative Medicine (CNRM) under the auspices of the Henry M. Jackson Foundation (HJF). DB was also supported in part by the IRP of the National Institute on Aging (NIA). Fabrication of the MRI phantoms was conducted as part of a user project at the Center for Nanophase Materials Sciences (CNMS), which is a US Department of Energy, Office of Science User Facility, Oak Ridge National Laboratory.

Funding information

Intramural Research Program; National Institute of Child Health and Human Development; Center for Neuroscience and Regenerative Medicine; National Institute of General Medical Sciences, Grant/Award Number: K99GM140338-01

REFERENCES

1. Komlosh ME, Özarslan E, Lizak MJ, et al. Mapping average axon diameters in porcine spinal cord white matter and rat corpus callosum using d-PFG MRI. Neuroimage. 2013;78:210–216. [PubMed: 23583426]
2. Avram L, Özarslan E, Assaf Y, Bar-Shir A, Cohen Y, Basser PJ. Three-dimensional water diffusion in impermeable cylindrical tubes: theory versus experiments. NMR Biomed. 2008;21:888–898. [PubMed: 18574856]
3. Assaf Y, Basser PJ. Composite hindered and restricted model of diffusion (CHARMED) MR imaging of the human brain. Neuroimage. 2005;27:48–58. [PubMed: 15979342]
4. Jensen JH, Helpern JA, Ramani A, Lu H, Kaczynski K. Diffusional kurtosis imaging: the quantification of non-gaussian water diffusion by means of magnetic resonance imaging. Magn Reson Med. 2005;53:1432–1440. [PubMed: 15906300]
5. Özarslan E, Koay CG, Shepherd TM, et al. Mean apparent propagator (MAP) MRI: a novel diffusion imaging method for mapping tissue microstructure. Neuroimage. 2013;78:16–32. [PubMed: 23587694]
6. Keenan KE, Ainslie M, Barker AJ, et al. Quantitative magnetic resonance imaging phantoms: a review and the need for a system phantom. Magn Reson Med. 2018;79:48–61. [PubMed: 29083101]

7. Kerstin D, Bernd LF, Marco B, Peter B, Anselm KT. Experimental determination of pore shapes using phase retrieval from q-space NMR diffraction. Phys Rev E. 2018;97:1–12.
8. Cheng Y, Cory DG. Multiple scattering by NMR. J Am Chem Soc. 1999;121:7935–7936.
9. Özarslan E, Shemesh N, Basser PJ. A general framework to quantify the effect of restricted diffusion on the NMR signal with applications to double pulsed field gradient NMR experiments. J Chem Phys. 2009;130:104702. [PubMed: 19292544]
10. Grebenkov DS. Multiple correlation function approach: rigorous results for simple geometries. Diff Fundam. 2007;5:1–34.
11. Komlosh ME, Horkay F, Freidlin RZ, Nevo U, Assaf Y, Basser PJ. Detection of microscopic anisotropy in gray matter and in a novel tissue phantom using double pulsed gradient spin echo MR. J Magn Reson. 2007;189:38–45. [PubMed: 17869147]
12. Shemesh N, Özarslan E, Adiri T, Basser PJ, Cohen Y. Noninvasive bipolar double-pulsed-field-gradient NMR reveals signatures for pore size and shape in polydisperse, randomly oriented, inhomogeneous porous media. J Chem Phys. 2010;133:044705. [PubMed: 20687674]
13. Komlosh ME, Benjamini D, Barnett AS, et al. Anisotropic phantom to calibrate high-q diffusion MRI methods. J Magn Reson. 2017;275:19–28. [PubMed: 27951427]
14. Nilsson M, Larsson J, Lundberg D, et al. Liquid crystal phantom for validation of microscopic diffusion anisotropy measurements on clinical MRI systems. Magn Reson Med. 2018;79:1817–1828. [PubMed: 28686785]
15. Komlosh ME, Özarslan E, Lizak MJ, et al. Pore diameter mapping using double pulsed-field gradient MRI and its validation using a novel glass capillary array phantom. J Magn Reson. 2011;208:128–135. [PubMed: 21084204]
16. Fieremans E, De Deene Y, Delputte S, Özdemir MS, Achten E, Lemahieu I. The design of anisotropic diffusion phantoms for the validation of diffusion weighted magnetic resonance imaging. Phys Med Biol. 2008;53:5405–5419. [PubMed: 18765890]
17. Vellmer S, Edelhoff D, Suter D, Maximov II. Anisotropic diffusion phantoms based on microcapillaries. J Magn Reson. 2017;279:1–10. [PubMed: 28410460]
18. Suzuki M, Moriya S, Hata J, Tachibana A, Senoo A, Niitsu M. Development of anisotropic phantoms using wood and fiber materials for diffusion tensor imaging and diffusion kurtosis imaging. Magn Reson Mate Phys Biol Med. 2019;32:539–547.
19. Ho CY, Deardorff R, Kralik SF, West JD, Wu YC, Shih CS. Comparison of multi-shot and single shot echo-planar diffusion tensor techniques for the optic pathway in patients with neurofibromatosis type 1. Neuroradiology. 2019;61:431–441. [PubMed: 30684113]
20. Fan Q, Nummenmaa A, Witzel T, et al. Axon diameter index estimation independent of fiber orientation distribution using high-gradient diffusion MRI. Neuroimage. 2020;222:117197. [PubMed: 32745680]
21. Basser PJ, Mattiello J, LeBihan D. MR diffusion tensor spectroscopy and imaging. Biophys J. 1994;66:259–267. [PubMed: 8130344]
22. Pierpaoli C, Walker L, Okan Irfanoglu M, et al. TORTOISE: an integrated software package for processing of diffusion MRI data. Joint Annual Meeting ISMRM-ESMRMB. 2010; Stockholm, Sweden. Abstract 1597.
23. Okan Irfanoglu M, Nayak A, Jenkins J, Pierpaoli C. TORTOISE v3: improvements and new features of the NIH diffusion MRI processing pipeline. 25th Annual Meeting and Exhibition ISMRM. 2017; Honolulu, HI. Abstract 3540.
24. Benjamini D, Komlosh ME, Basser PJ, Nevo U. Nonparametric pore size distribution using d-PFG: comparison to s-PFG and migration to MRI. J Magn Reson. 2014;246:36–45. [PubMed: 25064269]
25. Komlosh ME, Benjamini D, Hutchinson EB, et al. Using double pulsed-field gradient MRI to study tissue microstructure in traumatic brain injury (TBI). Microporous Mesoporous Mater. 2018;269:156–159. [PubMed: 30337835]
26. Özarslan E, Basser PJ. Microscopic anisotropy revealed by NMR double pulsed field gradient experiments with arbitrary timing parameters. J Chem Phys. 2008;128:154511. [PubMed: 18433239]

27. Herberthson M, Yolcu C, Knutsson H, Westin CF, Özarslan E. Orientationally-averaged diffusion-attenuated magnetic resonance signal for locally-anisotropic diffusion. Sci Rep. 2019;9:4899. [PubMed: 30894611]
28. Yolcu C, Herberthson M, Westin CF, Özarslan E. Magnetic resonance assessment of effective confinement anisotropy with orientationally-averaged single and double diffusion encoding. In: Evren Ö, Thomas S, Eugene Z, Andrea F, eds. Anisotropy Across Fields and Scales. Springer International Publishing; 2021:203–223.
29. Benjamini D, Basser PJ. Use of marginal distributions constrained optimization (MADCO) for accelerated 2D MRI relaxometry and diffusometry. J Magn Reson. 2016;271:40–45. [PubMed: 27543810]
30. Pajevic S, Pierpaoli C. Color schemes to represent the orientation of anisotropic tissues from diffusion tensor data: application to white matter fiber tract mapping in the human brain. Magn Reson Med. 1999;42:526–540. [PubMed: 10467297]
31. Bottomley PA. Spatial localization in NMR spectroscopy in vivo. Ann N Y Acad Sci. 1987;508:333–348. [PubMed: 3326459]
32. Assaf Y, Freidlin RZ, Rohde GK, Basser PJ. New modeling and experimental framework to characterize hindered and restricted water diffusion in brain white matter. Magn Reson Med. 2004;52:965–978. [PubMed: 15508168]
33. Nilsson M, Lasič S, Drobnjak I, Topgaard D, Westin CF. Resolution limit of cylinder diameter estimation by diffusion MRI: the impact of gradient waveform and orientation dispersion. NMR Biomed. 2017;30:e3711. [PubMed: 28318071]
34. Tang L, Lee NY. A facile route for irreversible bonding of plastic-PDMS hybrid microdevices at room temperature. Lab Chip. 2010;10:1274–1280. [PubMed: 20445880]
35. Neuman CH. Spin echo of spins diffusing in a bounded medium. J Chem Phys. 1974;60:4508–4511.
36. Codd SL, Callaghan PT. Spin echo analysis of restricted diffusion under generalized gradient waveforms: planar, cylindrical, and spherical pores with wall relaxivity. J Magn Reson. 1999;137:358–372. [PubMed: 10089170]
37. Vangelderen P, DesPres D, Vanzijl PCM, Moonen CTW. Evaluation of restricted diffusion in cylinders. Phosphocreatine in rabbit leg muscle. J Magn Reson B. 1994;103:255–260. [PubMed: 8019777]
38. Benjamini D, Komlosh ME, Basser PJ. Imaging local diffusive dynamics using diffusion exchange spectroscopy MRI. Phys Rev Lett. 2017;118:158003. [PubMed: 28452522]
39. Cai TX, Benjamini D, Komlosh ME, Basser PJ, Williamson NH. Rapid detection of the presence of diffusion exchange. J Magn Reson. 2018;297:17–22. [PubMed: 30340203]
40. Wapler MC, Leupold J, Dragonu I, Von Elverfeld D, Zaitsev M, Wallrabe U. Magnetic properties of materials for MR engineering, micro-MR and beyond. J Magn Reson. 2014;242:233–242. [PubMed: 24705364]
41. Bhagwandien R, Moerland MA, Bakker CJG, Beersma R, Lagendijk JJW. Numerical analysis of the magnetic field for arbitrary magnetic susceptibility distributions in 3D. Magn Reson Imaging. 1994;12:101–107. [PubMed: 8295497]
42. Terenzi C, Dvinskikh SV, Furó I. Wood microstructure explored by anisotropic 1H NMR line broadening: experiments and numerical simulations. J Phys Chem B. 2013;117:8620–8632. [PubMed: 23772558]
43. Lee J, Shmueli K, Fukunaga M, et al. Sensitivity of MRI resonance frequency to the orientation of brain tissue microstructure. Proc Natl Acad Sci. 2010;107:5130–5135. [PubMed: 20202922]
44. Wharton S, Bowtell R. Fiber orientation-dependent white matter contrast in gradient echo MRI. Proc Natl Acad Sci. 2012;109:18559–18564. [PubMed: 23091011]
45. Wang Z, Bovik AC, Sheikh HR, Simoncelli EP. Image quality assessment: from error visibility to structural similarity. IEEE Trans Image Process. 2004;13:600–612. [PubMed: 15376593]
46. Henriques RN, Palombo M, Jespersen SN, Shemesh N, Lundell H, Ianuş A. Double diffusion encoding and applications for biomedical imaging. J Neurosci Methods. 2021;348: 108989. [PubMed: 33144100]

47. Özarslan E, Shemesh N, Koay CG, Cohen Y, Basser PJ. Nuclear magnetic resonance characterization of general compartment size distributions. New J Phys. 2011;13:15010.

48. Jelescu IO, De Skowronski A, Geffroy F, Palombo M, Novikov DS. Neurite exchange imaging (NEXI): a minimal model of diffusion in gray matter with inter-compartment water exchange. Neuroimage. 2022;256:119277. [PubMed: 35523369]

49. Callaghan PT, Furo I. Diffusion-diffusion correlation and exchange as a signature for local order and dynamics. J Chem Phys. 2004;120:4032–4038. [PubMed: 15268569]

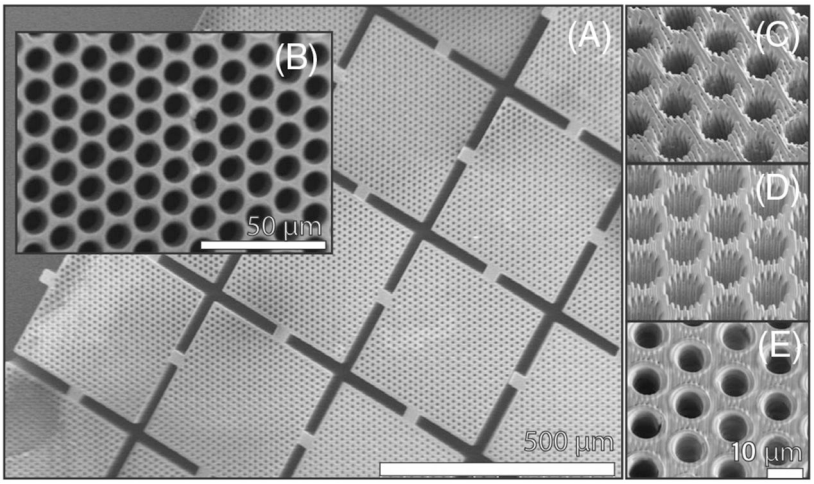

FIGURE 1.

Scanning electron microscopy (SEM) images of a final optimized array (A,B) and images (C,D,E) acquired from singular blocks printed with the conditions provided in Table 1. The white lines indicate the scale bars.

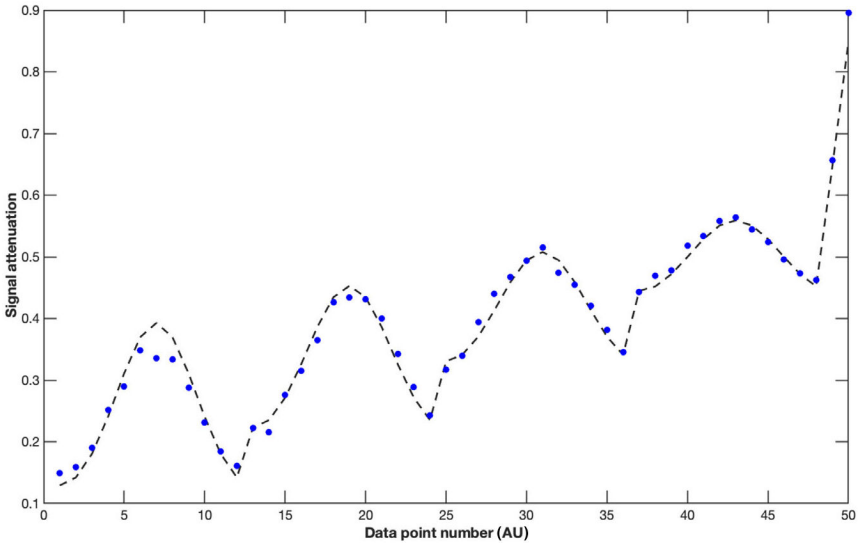

FIGURE 2.

The experimental signal intensity and the resulting fit (mixed Gaussian and restricted diffusion model)[32] are plotted against the data points, each of which corresponds to a different set of pulse gradient strength and direction, with bulk diffusivity of 2.0×10^{-9} m^2/s. The diameter for the aligned cylinders was estimated to be 8.38 μm, and the fraction of the free-water signal was estimated to be $f_g = 0.38$.

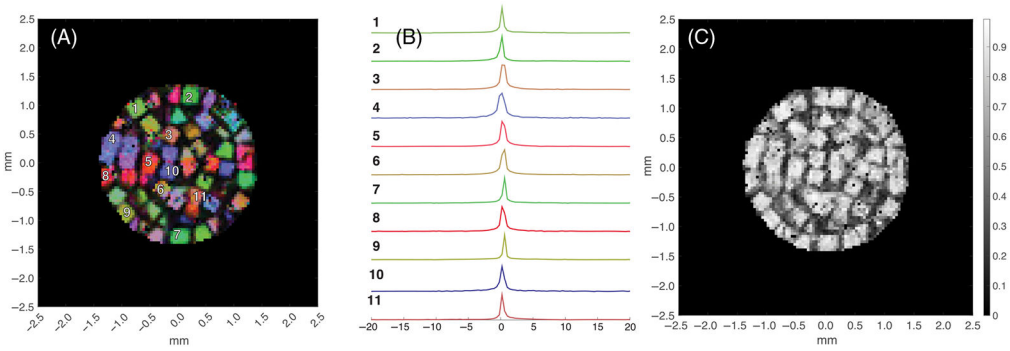

FIGURE 3.

Panel A is the Diffusion-Encoded Color (DEC) MRI map from a TORTOISE analysis obtained with 50 μm^3 isotropic voxels. The letters on the left image represent voxels containing blocks with different orientations, for which Point RESolved Spectroscopy (PRESS) ^1H spectra are also obtained. The corresponding spectra are shown in B plotted against ω_0, the Larmor frequency (in ppm) and resulted in a SD of 0.2 ppm or 60 Hz, within the normal shimming linewidth achievable with this instrument. If there were significant susceptibility artifacts, one would expect to see the Larmor frequency vary with the orientation of the capillaries with respect to the main magnetic field direction. Panel C is an axial slice of the fractional anisotropy (FA) map, with 50×50×50 μm^3 voxel size, demonstrating that diffusion in each block is highly anisotropic with FA > 0.75.

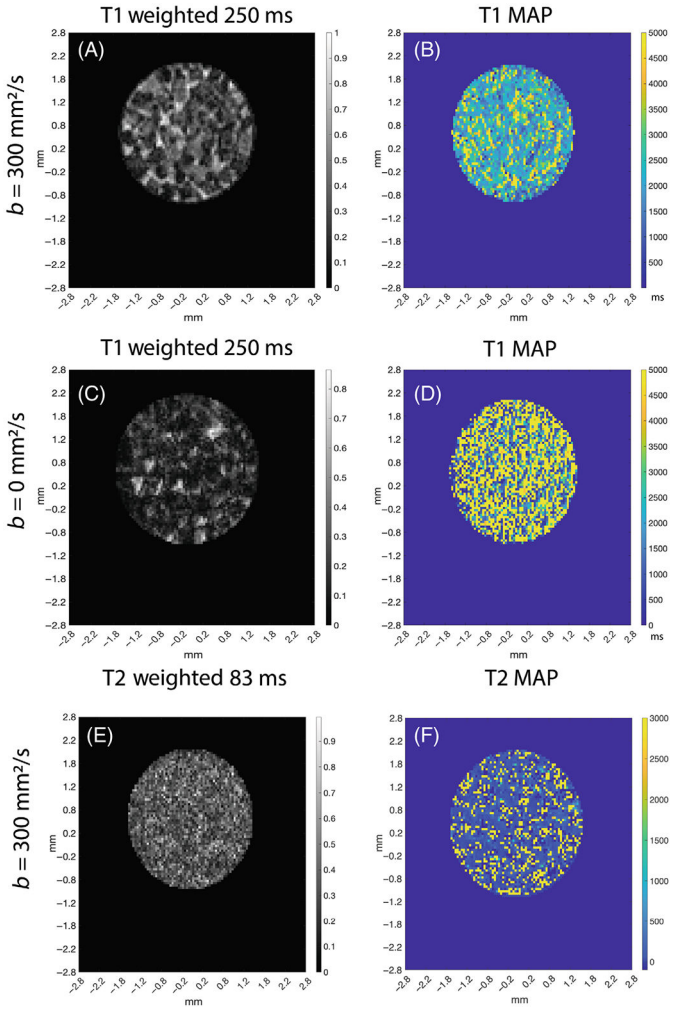

FIGURE 4.

Axial slices of echo-planar imaging (EPI) acquisition (C and D) images and diffusion-weighted (DW) (A and B) EPI experiments with Inversion Recovery T_1 preparation, acquired with eight segments, where a custom Matlab code employing a single time the constant model was used to generate the T_1 MAP (B and D) and the weighted images (A and C) displayed have inversion times 250 ms. Axial slices of DW (E and F) EPI experiments with T_2 weighted imparted by varying the echo time, acquired with 8-segments, where custom Matlab code employing a single time the constant model was used to generate the T_2 MAP (F) and the weighted images (E and C) displayed have echo time of 83 ms. The images show that restriction of water diffusion in the blocks' capillary arrays shortens the voxel's effective T_1 independent of the orientation of the cube while water outside the cube has a significantly longer T_1. Also, it shows that the T_2 of the water is long and not the T_2 of the polymer material. This contrast is enhanced when only the diffusing water molecules are considered (A, B, E, and F).

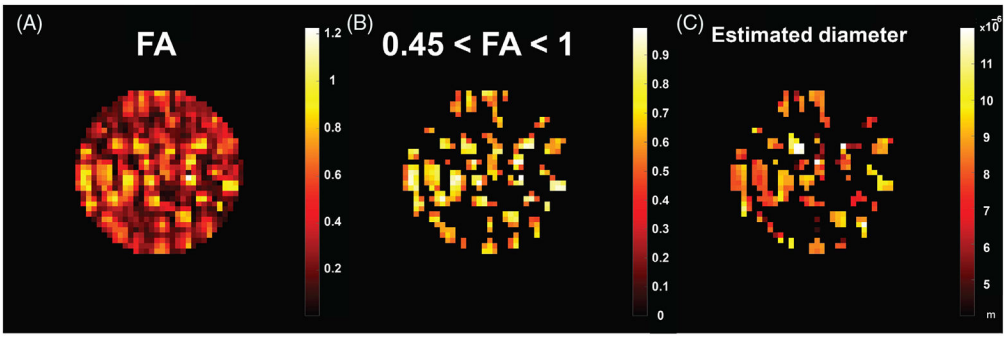

FIGURE 5.

The same axial slices were acquired using an echo-planar imaging (EPI) sequence where the number of segments was varied from 2 (A), 4(B), and 6(C) segments, with TE = 54 ms. The three-dimensional voxel size is 50 μm^3. The relative structural similarity index measures of images B and C to the first image A are 0.9984 and 0.9661, respectively.

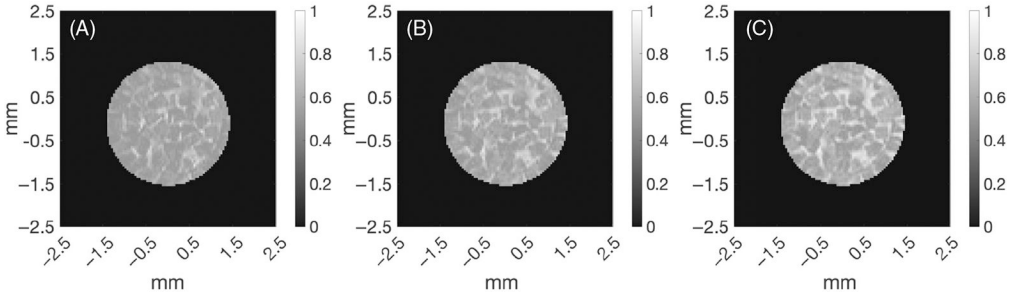

FIGURE 6.

Axial slice double pulsed field gradient experiment at 100-micron resolution shows the calculated fractional anisotropy map (A), the thresholded map (B), and the resulting estimated diameter map (C).

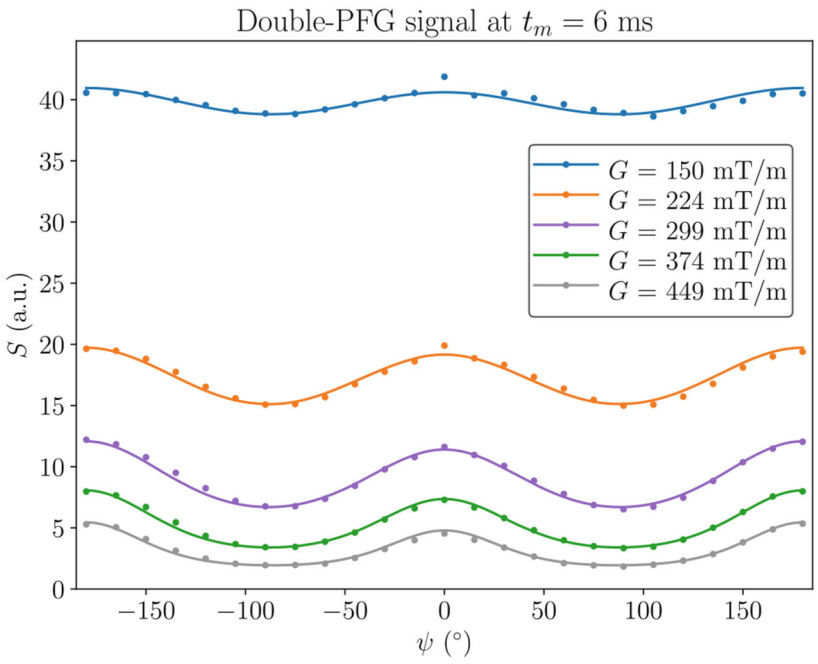

FIGURE 7.

All signals from all voxels were combined for the numerical analysis of the double-pulsed field gradient experiments at t_m = 6 ms. Here we depict experimental data (dots) and the numerical fits (lines) for the echo amplitude (E) as a function of the angle between the first and second gradient pulse (Ψ) at various gradient strengths.

TABLE 1

Printing conditions.

Sample	Slicing (mm)	Hatching (mm)	Laser scanning velocity (mm/s)	Power (%)	Contouring distance (mm)	Printing time per block (min)
A	1	0.8	50	60	n/a	8
B	1	0.8	50	60	n/a	9
C	1	0.7	50	60	0.3	16

TABLE 2

Estimated parameter values.

Diffusion experiments	**Cylinder diameter (μm)**	**Free water fraction**
Double pulsed field gradient on aligned cylinders	8.38	0.38
Double pulsed field gradient on randomly oriented cylinders	7.80	0.60
Relaxation experiments	**Relaxation time**	**Estimate (s)**
Multigradient echo	T_2^*	0.3548
Multislice multi-echo sequence	T_2	0.457
IRFLASH3D	T_1	0.97

TABLE 3

Frequency perturbation in a hollow cylinder for isotropic magnetic susceptibility (χ), with $\Delta\chi = \chi_{H_2O} - \chi_{PMMA}$ used below.

$r < r_i$	$r_i < r < r_o$	$r > r_o$
0	$\Delta\chi\frac{1}{2}\left(\cos^2\theta - \frac{1}{3} - \sin^2\theta\cos 2\phi\left(\frac{r_i^2}{r^2}\right)\right)$	$\Delta\chi\frac{\sin^2\theta\cos 2\phi}{2}\left(\frac{r_o^2 - r_i^2}{r^2}\right)$